FULL PAPER

Wearable Pseudocapacitors

ADVANCED
ENERGY
MATERIALS

www.advenergymat.de

Novel Sub-5 nm Layered Niobium Phosphate Nanosheets for High-Voltage, Cation-Intercalation Typed Electrochemical Energy Storage in Wearable Pseudocapacitors

Zeyi Wu, Le Jiang, Wenchao Tian, Yanan Wang, Yingchang Jiang, Qinfen Gu, and Linfeng Hu*

Layered niobium phosphates have been considered very promising energy storage materials because of their high theoretical operating voltage window and the rich oxidation states of niobium. However, their development has been stymied by the phase-controlled synthesis due to the insolubility of niobium sources except in concentrated hydrofluoric (HF) acid systems. Herein, a new avenue is opened for layered acid niobium phosphate ($2NbOPO_4 \cdot H_3PO_4 \cdot H_2O$) synthesis in a mild oxalic acid system. Taking advantage of this strategy, in situ growth of sub-5 nm $2NbOPO_4 \cdot H_3PO_4 \cdot H_2O$ nanosheet (NPene) arrays on conductive carbon fiber cloth (CFC) substrates is achieved as self-standing electrodes for solid-state supercapacitors. Interestingly, the NPene@CFC electrode exhibits a typical cation (H^+ or Li^+)-intercalation kinetics with a wide potential window of 0–1.0 V in aqueous electrolytes. Given the wide potential window and highly exposed active surface, the solid-state asymmetric supercapacitors constructed from such a NPenes@CFC electrode display a high working potential of 2.0 V, energy density of 122.2 W h kg^{-1} at a power density of 589.7 W kg^{-1}, cycle stability with a capacitance retention of 94.2% after 10 000 cycles, and also outstanding flexible and wearable characteristics.

1. Introduction

The rapid development of portable and wearable smart electronics results in an urgent demand of flexibility and miniaturization of electrochemical energy devices.[1–3] Wearable solid-state supercapacitors (WSSPs) attract considerable attention for wearable, on-chip energy storage recently owing to ultrahigh power density, long-term cycle stability, aqueous electrolyte system for environmental friendliness, and high

safety.[4–7] A series of advanced progress has been made toward flexible supercapacitor design in recent years, including micro-SCs based on serpentine interconnections,[8] fiber-shaped SCs,[9] and the devices based on new crumpled-graphene papers,[10] tricot weave,[11] hierarchically buckled sheah-core fibers.[12] Nevertheless, the practical application of WSSPs is still limited by their low energy density.[13] According to the equation of energy density $E = 1/2\ C\ V^2$, for a given supercapacitor (SC), the energy density highly depends on the specific capacitance (C) and operating voltage window (V).[13] Given by this equation, the energy density is proportional to the square of operating voltage window. In general, the electrochemical stability window of most energy-storage materials is less than 0.8 V in aqueous electrolytes due to the water splitting at 1.23 V, and high-voltage materials is highly desired to enhance the energy density.[14]

Most recently, layered polyanionic phosphates, such as $VOPO_4$, $Na_3V_2(PO_4)_3$, $NaVOPO_4$, $KVPO_4F$, and $KVOPO_4$, have been considered as promising electrode materials for energy storage because of their high thermal and structural stability.[15] More importantly, it has been theoretically predicted a much higher potential ($\approx$1.0 V in aqueous electrolyte) in layered phosphates than in most of the traditional pseudocapacitive materials due to the enhanced iconicity of metal–oxygen bond with the existence of $[PO_4]^{3-}$ group.[16–19] Meanwhile, niobium (Nb) is an important transition metal element with rich oxidation states (Nb^{3+}, Nb^{4+}, and Nb^{5+}) for potential electrochemical energy storage. A unique Li^+-intercalation pseudocapacitance has been found in T-Nb_2O_5 (40 μm thick) electrode, which holds a great perspective on the development of electrochemical electrodes.[20,21] Especially, the pseudocapacitance occurs in the T-Nb_2O_5 bulk rather than the surface or near-surface of the electrode, resulting high specific capacitances and energy density.[20] These interesting results inspire us to consider whether Nb atoms could be intercalated into the layered polyanionic phosphate to form layered niobium phosphate as high-performance electrode materials for WSSPs.

Z. Y. Wu, L. Jiang, W. C. Tian, Y. N. Wang, Dr. Y. C. Jiang,
Prof. L. F. Hu
Department of Materials Science
Fudan University
Shanghai 200433, P. R. China
E-mail: linfenghu@fudan.edu.cn
Dr. Q. F. Gu
Australian Synchrotron (ANSTO)
800 Blackburn Road, Clayton 3168, Australia
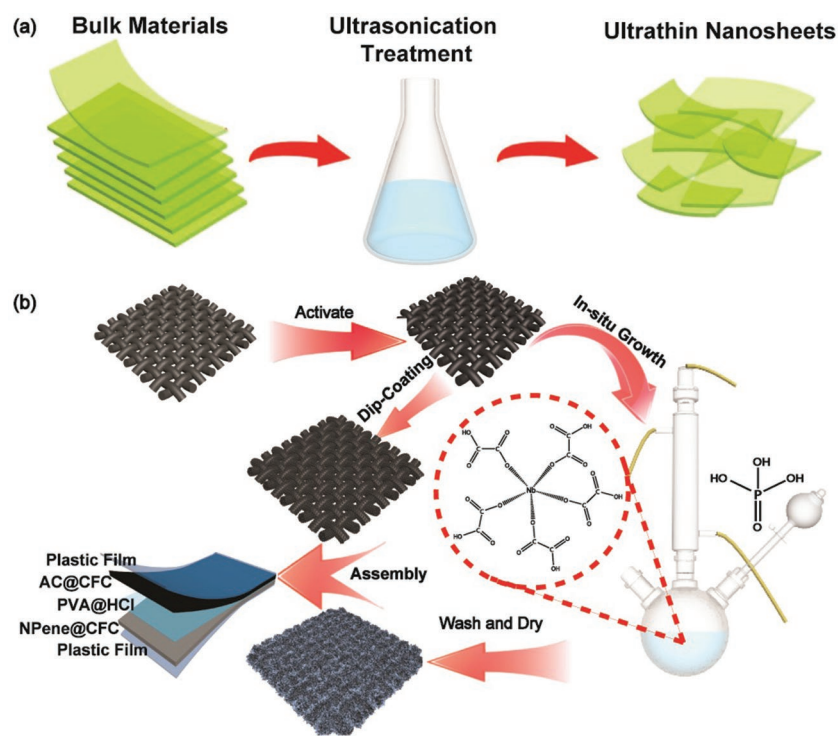
Scheme 1. Schematic representations of a) liquid exfoliation of $2NbOPO_4 \cdot H_3PO_4 \cdot H_2O$ bulk. b) The in situ growth and assembly process of wearable, asymmetric supercapacitor from these niobium phosphate nanosheets.

However, to the best of our knowledge, the electrochemical properties of layered niobium phosphate have never been reported up to date, and the main challenge lies in the difficulty on the material synthesis. Note that $VOPO_4$ and $NaVOPO_4$ have been prepared by a wet-chemical refluxing routine of the aqueous mixture including V_2O_5 and H_3PO_4.[16,22,23] Unfortunately, completely different from V_2O_5, niobium (Nb) oxides are hardly dissolved in most of the strong acid solution. Only reported by Sanzt et al. in 1987, the formation of layered niobium phosphate was realized in a concentrated hydrofluoric (HF) acid system.[24] Known that concentrated HF is highly corrosive and toxic, it gives rise to difficulty of chemical synthesis due to the rigorous requirement of reaction container and also the generation of large quantities of chemical waste. Furthermore, it leads to the impossibility of in situ growth of layered niobium phosphates on various flexible substrates, which is usually considered as a crucial pathway to reduce electrode interface resistance and improve charge/ion transport for WSSPs. Other typical niobium source, such as niobium (V) chloride ($NbCl_5$), is rather unstable and also requires a strong acid environment for its dissolution.[25]

In this work, we break from the conventional HF-strategy for the synthesis of layered niobium phosphates and demonstrate that layered acid niobium phosphate ($2NbOPO_4 \cdot H_3PO_4 \cdot H_2O$) nanoplates can be rapidly produced in a mild oxalic acid system by a facile refluxing routine using $Nb(C_2HO_4)_5$ as the niobium source (**Scheme 1**). Then, in situ growth of sub-5 nm $2NbOPO_4 \cdot H_3PO_4 \cdot H_2O$ nanosheet (niobium phosphene, NPene) arrays on conductive carbon fiber cloth (CFC) substrate

was successfully achieved as a flexible, self-standing electrode for WSSPs. Interestingly, the resulting NPene@CFC electrode exhibits a typical cation (H^+ or Li^+)-intercalation electrochemical energy storage with a wide potential window of 0–1.0 V in aqueous electrolyte (vs Ag/AgCl electrode). The flexible, quasi-solid-state asymmetric supercapacitors constructed from the resulting NPenes@CFC electrode displayed a high working potential of 2.0 V, energy density of 122.2 W h kg^{-1} at a power density of 589.7 W kg^{-1}. Our findings open up a new avenue and a significant step toward exploring cation-intercalation typed niobium phosphate materials for high-performance flexible energy storage device.

2. Results and Discussion

Pure $2NbOPO_4 \cdot H_3PO_4 \cdot nH_2O$ (JCPDS 47-0151) was prepared in an oxalic acid system by a facile oil-bath refluxing routine (**Figure 1**a). The sample consists of numerous platelets with irregular shape and lateral size at a range of 2 µm (Figure 1b). Various Nb/P ratios (from 1:1 to 1:20) in the starting reactant all produce pure $2NbOPO_4 \cdot H_3PO_4 \cdot nH_2O$ phase. However, higher Nb/P ratios than 1:2 results in the improvement of crystallinity. Note that the (002) diffraction peaks gradually increases with the increases of Nb/P ratio, suggesting that the crystallographic orientation is much more prominent along [001] direction (Figure S1, Supporting Information). Meanwhile, the lateral size of the platelets gradually decreases as the Nb/P ratio increases (Figure S2, Supporting Information). The crystallographic water content in this compound was verified as $n = 1$ by thermogravimetric analysis (TGA) (Figure S3, Supporting Information). We propose that the reaction during the refluxing process should be

$$2\left[Nb(C_2HO_4)_5\right] + 3H_3PO_4 + 5O_2 \rightarrow 2NbOPO_4 \cdot H_3PO_4 \cdot H_2O + 20CO_2 \uparrow + 7H_2O$$
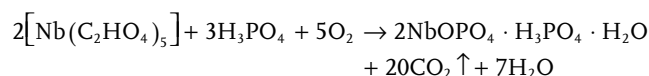
The crystal structure was solved by the combined Rietveld refinements of high-resolution synchrotron X-ray powder diffraction (SXRPD) data and density functional theory (DFT) calculations. All the diffraction peaks could be indexed as a triclinic structure in $P1$ space group with $a = 6.485$ Å, $b = 6.415$ Å, $c = 16.18$ Å, $\alpha = 90.11°$, $\beta = 95.91°$, and $\gamma = 90.95°$ (Figure S4, Supporting Information). As seen from SXRPD data, the asymmetry peak shape and stepped background are introduced by heavy stacking fault and interlayer offset with weak layer to layer bonding. The crystallographic information and calculated atomic coordinates are listed in Table S1 in the Supporting Information. This is the first reported crystal structure of $2NbOPO_4 \cdot H_3PO_4 \cdot H_2O$ compound since its discovery in 1990.[26] The layered structure consists of [$NbOPO_4$] layers with H_3PO_4 and H_2O molecules residing in the gallery (Figure 1d,e).
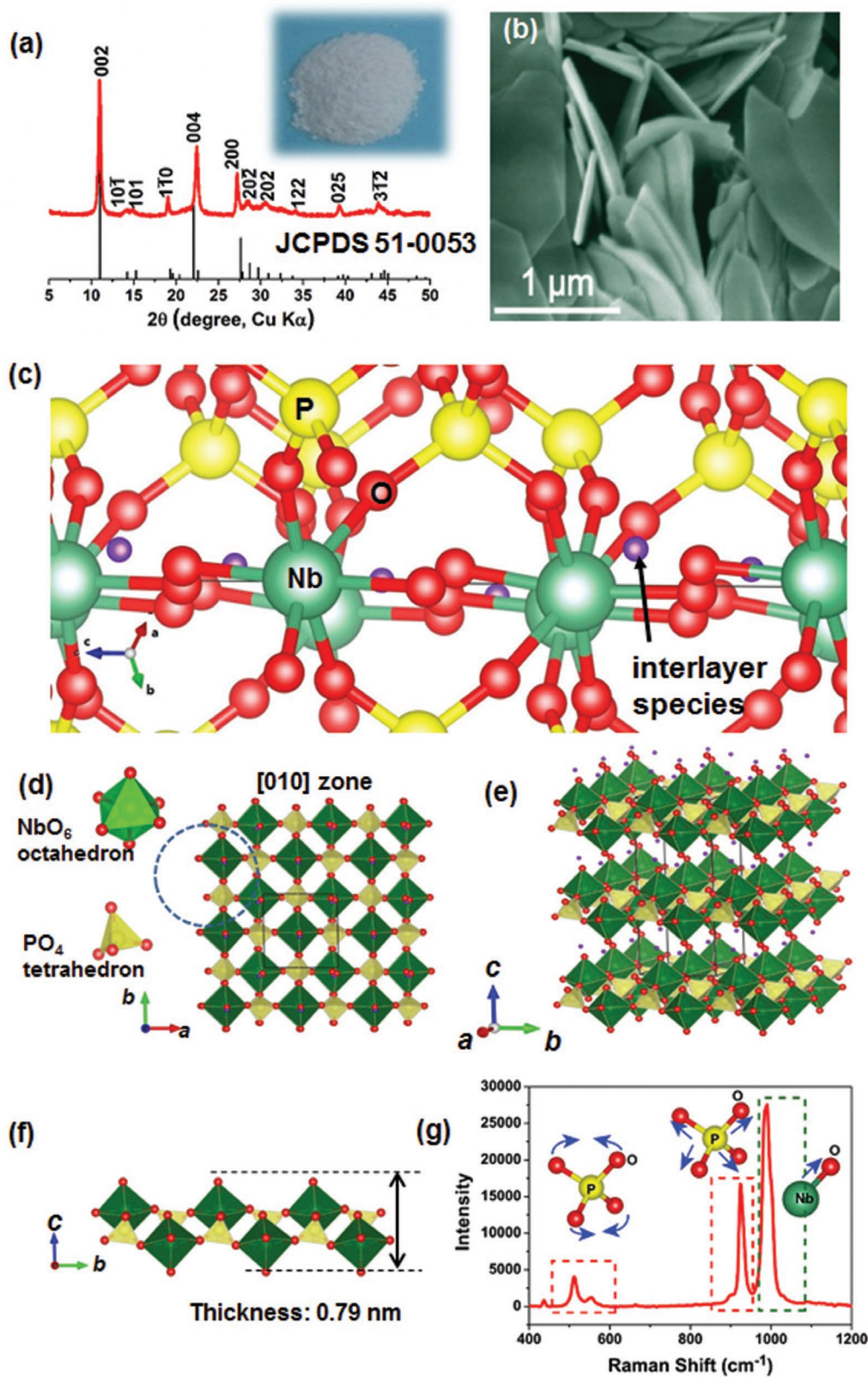
Figure 1. Morphology and crystal structure information of $2NbOPO_4 \cdot H_3PO_4 \cdot H_2O$. a) The XRD pattern (powder photograph inserted) and b) SEM image of the as-prepared $2NbOPO_4 \cdot H_3PO_4 \cdot H_2O$ bulk. c) The local coordination of Nb and P atoms in the $2NbOPO_4 \cdot H_3PO_4 \cdot H_2O$ crystal. d) The top view of $2NbOPO_4 \cdot H_3PO_4 \cdot H_2O$ unit cell. e) 3D layered crystal structure of $2NbOPO_4 \cdot H_3PO_4 \cdot H_2O$ crystal. f) The crystallographic thickness (D_0) model of a $[NbOPO_4]$ atomic monolayer. g) Raman spectrum of as-prepared $2NbOPO_4 \cdot H_3PO_4 \cdot H_2O$.

The in-plane atomic arrangement of layers consist the chains of corner-shared, slightly distorted $[NbO_6]$ octahedron and $[PO_4]$ tetrahedron that run parallel to the *c*-axis (Figure 1c). The six O⋯Nb distances in the slightly distorted $[NbO_6]$ octahedron are 1.89(3), 1.94(2), 1.99(2), 2.00(0), 2.02(2), and 2.06(5) Å, respectively. Meanwhile, the O⋯P distance in $[PO_4]$ tetrahedron is 1.54(1) Å. The site assignments of $[NbO_6]$ octahedron and $[PO_4]$ tetrahedron produce alternating rows, which form layers parallel to the *ab* plane. The crystallographic thickness (D_0) of a $[NbOPO_4]$ atomic monolayer projected along [010] can be calculated as 0.789 nm (Figure 1f). Raman spectra of $2NbOPO_4 \cdot H_3PO_4 \cdot H_2O$ reveal the symmetric stretching vibrations of $[PO_4]^{3-}$ at around 937 cm^{-1} and symmetric bending modes of $[PO_4]^{3-}$ at 541, and 579 cm^{-1}, respectively.[27,28] The sharp peak at 950 cm^{-1} demonstrates the existence of stretching vibrations from Nb=O bond in the present product (Figure 1g). The DFT calculation was performed to deeply understand the intrinsic properties, indicating a semiconductor nature with a direct energy gap of 2.1 eV (Figure S5, Supporting Information). Valence electron localization function analysis further suggests the intrinsic strong interaction within the intralayer and weak van der Waals interactions among $[NbOPO_4]$ adjacent layers (Figure S6, Supporting Information). A series of thermal analysis measurements were also carried out to confirm the structure information of the as-synthesized $2NbOPO_4 \cdot H_3PO_4 \cdot H_2O$. X-ray diffraction (XRD) patterns of the products after calcination of $2NbOPO_4 \cdot H_3PO_4 \cdot H_2O$ at various temperatures indicates the phase stability until 400 °C (Figure S7, Supporting Information).

Annealing in air at 900 °C results in pure $Nb_{1.91}P_{2.82}O_{12}$ phase (JCPDS 51-1738). Further confirmed by Rietveld refinement of in situ XRPD patterns (Figure S8, Supporting Information) more clearly, the crystallographic water in $2NbOPO_4 \cdot H_3PO_4 \cdot H_2O$ was completely removed at 550 °C.

Single-crystal microdiffraction data based on an individual $2NbOPO_4 \cdot H_3PO_4 \cdot H_2O$ platelets (crystal size: ≈3 µm) conducted on MX2 beamline at Australian Synchrotron confirms the fine polycrystalline nature of individual platelets (Figure S9, Supporting Information). This result suggests the layered-stacking of atomic-thin sheets in such individual platelets and the possible exfoliation of the bulk. After an ultrasonic treatment of the $2NbOPO_4 \cdot H_3PO_4 \cdot H_2O$ platelets aqueous dispersion (10 mg·mL^{-1}) for 10–20 mins, milk-like colloidal solution can be yielded. This routine is easy to scale up, and we have easily large-scale produced 5.0 L aqueous colloidal solution with a concentration of 10.0 mg mL^{-1} (**Figure 2**a). A clear Tyndall light scattering was observed in the as-prepared colloidal solution (Figure 2b), indicating the presence of well-dispersed thin-layers in water phase. The resulting colloidal suspension was very stable without sediment for several months. However, after addition of a small amount of NaCl (3.0 M) aqueous solution, white flocculent-like sediment appeared immediately, demonstrating the charged nature of our colloidal suspension (Figure 2c). Transmission electron microscopy (TEM) image and the corresponding selected area electron diffraction (SAED) pattern in **Figure 3**d–f show a large number of semitransparent 2D sheet-like objects with a single-crystal
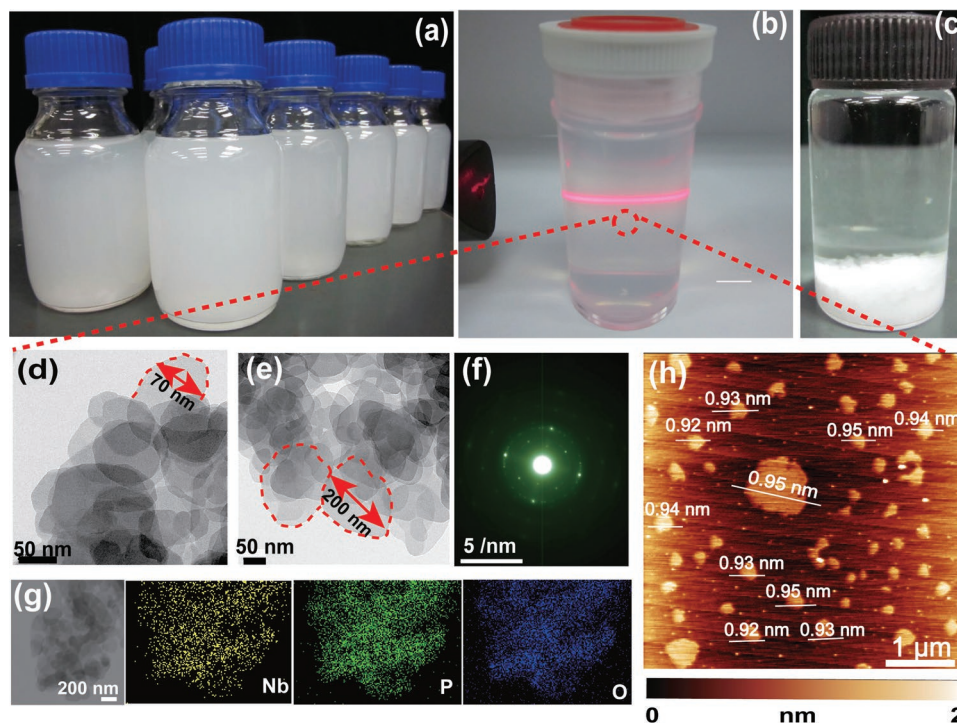
Figure 2. Nature and characterization of the dispersive NPene nanosheets. a) Large-scaled synthesis of single-layer nanosheet suspension. b) Photograph of the nanosheet suspension illuminated by the red light of a laser pointer. c) The instantaneous appearance of floccule sediment from the colloidal suspension by the addition of a low dose of NaCl aqueous solution. d,e) TEM images and f) the corresponding SAED pattern take from an individual nanosheet. g) EDX element maps of Nb, P, O element, respectively. h) AFM image and height profiles of the nanosheets.

ADVANCED
SCIENCE NEWS
www.advancedsciencenews.com

ADVANCED
ENERGY
MATERIALS
www.advenergymat.de

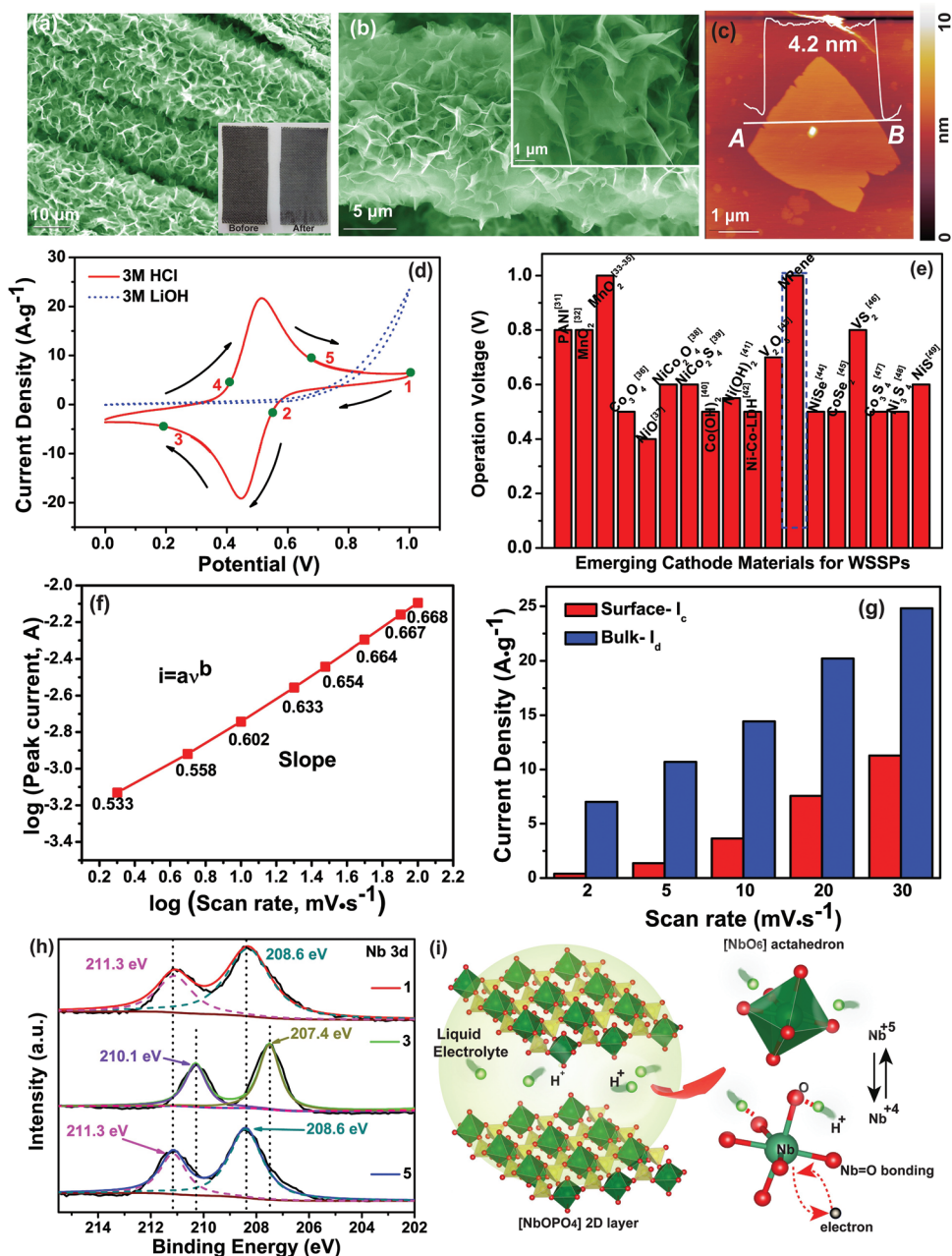**Figure 3.** In situ growth of NPene@CFC and its electrochemistry performance. a,b) Typical SEM images of as-grown NPene@CFC. The insert in (a) shows the apparent color change of CFC before and after the in situ growth. Insert in (b) shows a detailed SEM image of a selected area of the electrode. c) Typical AFM image and the height information of the as-grown NPene. d) CV profiles of the NPenes@CFC electrode in various electrolyte solutions at 10.0 mV s^{-1}. e) The bar chart in regard to the operation voltage of various cathode materials for WSSPs and that of NPene. f) The dependence of the peak current and the scan rate at the scan rate from 2.0 to 100.0 mV s^{-1}. g) Capacity contribution of surface pseudocapacitive effect and diffusion-controlled mechanism at a scan rate of 2, 5, 10, 20, and 30 mV·s^{-1}, respectively. h) Nb XPS spectra of the NPene@CFC electrode at three typical stage (1, 3, 5) during a complete scanning cycle. i) Schematic illustration of the pseudocapacitive kinetics process between H$^+$ and NPenes.

nature, which are metastable and easily transformed to an amorphous structure under long-time e-beam irradiation (Figure S10, Supporting Information). The Nb, O, and P elements are uniformly distributed through the nanosheets as shown in the corresponding energy dispersive spectrometer (EDS) element maps (Figure 2g). A tapping-mode atomic force microscopy (AFM) image shows numerous nanosheets with lateral dimensions of a few hundreds of nanometers (Figure 2h), the height profile of which reveals an ultrathin thickness of ≈1.0 nm. We propose a possible unilamellar [NbOPO$_4$] layer consisting of the chains of corner-shared of distorted [NbO$_6$] octahedron and [PO$_4$] tetrahedron based on the theoretical thickness of 0.79 nm (Figure 1f). As demonstrated from the zeta potential measurement (Figure S11,
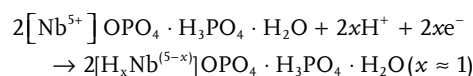
Supporting Information), the as-exfoliated nanosheet is negative charged, which agrees well with the appearance of flocculent-like sediment in 1c and should be attributed to the adsorption of negative $[PO_4]^{3-}$ groups on the surface. The optical absorption measurement indicates a blueshift of 0.37 eV of the absorption edge of the as-exfoliated nanosheets (Figure S12, Supporting Information). This can be ascribed to smaller-size nanostructures raise the conduction band and lower the valence band, resulting in a concomitant increase of the bandgap.[29,30] All the aforementioned results confirm that the layered $2NbOPO_4 \cdot H_3PO_4 \cdot H_2O$ bulk has been successfully exfoliated into atomically thin 2D materials.

Taking advantage of the mild-acid synthetic environment, the arrays of $2NbOPO_4 \cdot H_3PO_4 \cdot H_2O$ nanosheet (NPene) can be in situ grown on a flexible CFC substrate. The scanning electron microscopy (SEM) observation indicates that the CFC substrate is densely covered with flexible and ultrathin NPene arrays which are perpendicularly intersected and aligned on the surface of the CFC (Figure 3a,b). A sharp peak from the (00l) diffraction ($d = 8.03$ Å) of $2NbOPO_4 \cdot H_3PO_4 \cdot H_2O$ phase was detected in the XRD pattern after this growth (Figure S13, Supporting Information). The AFM image of an individual NPene taken from the as-grown arrays demonstrates the smooth surface and an atomic thickness of 4.2 nm (Figure 3c), corresponding to 3 sublayer structure of the $2NbOPO_4 \cdot H_3PO_4 \cdot H_2O$ crystal. The X-ray photoelectron spectroscopy (XPS) of the NPene@CFC electrode also confirms the chemical composition and states of the as-grown NPenes (Figure S14, Supporting Information). Subsequently, cyclic voltammetry (CV) measurements for the NPenes @CFC electrode were performed in a three-electrode cell configuration with different electrolyte solutions including alkaline LiOH (3.0 M), neutral LiCl (3.0 M), acidic HCl (3.0 M), H_2SO_4 (1.5 M), and the mixture of HCl (3.0 M)/LiCl (3.0 M), respectively. Alkaline LiOH electrolyte solution leads to almost no electrochemical performance of our NPene@CFC electrode (Figure 3d). Differently, the CV data in neutral LiCl electrolyte exhibits clear electrochemical response, and the best performances has been observed in HCl or H_2SO_4 solutions, of which a pair of the redox peaks approximately located at 0.42 and 0.57 V, respectively. (Figure 3d; Figure S15, Supporting Information). The reason should be ascribed to the decomposition of NPene in an alkaline condition and the rapid Faradaic pseudo-capacitance process activated by H^+ or Li^+. Due to the smaller size and faster ionic mobility of H^+ than that of Li^+, the electrochemical reaction is enhanced with the participation of H^+ in acidic electrolyte. The Nyquist plot of the NPene@CFC electrode shows the nearly negligible charge transfer resistance (R_{ct}) of the electrode, demonstrating the fast transportation procedure of ions (Figure S16, Supporting Information). The specific capacitance of the NPene@CFC electrode was 1421.6 F g^{-1} at the scan rate of 2 mV s^{-1} in HCl (3.0 M) electrolyte. More importantly, the operating potential window of the present NPene@CFC electrode in acid electrolyte is up to 1.0 V (Figure S17, Supporting Information), depicting a higher potential window than most of the other conventional materials for WSSPs (Figure 3e).[31–49]

Note that the CV curves show widely separated peaks associated with the redox of the metal centers involved in charge storage. In addition, the peak current in the CV curves generally obeys a power–law relationship with the sweep rate[50]

$$i = \alpha V^b$$

where a and b are adjustable values. Whereas b-value of 0.5 would indicate that the current is controlled by semi-infinite linear diffusion, a value of 1.0 indicates that the current is surface controlled. In our case, for sweep rates ranging from 2.0 to 100.0 mV s^{-1}, the b-value for peak current are 0.533, 0.558, 0.602, 0.633, 0.654, 0.664, 0.667, and 0.668, respectively, revealing a diffusion-controlled battery-type mechanism in the present energy storage system (Figure S18, Supporting Information; Figure 3f,g).[50] Ex situ XPS analysis of the electrode at different pseudocapacitive stages was performed to further clarify the electrochemical kinetics process clearly. The XPS peaks of Nb-3d$_{3/2}$ and Nb-3d$_{5/2}$ of initial state (stage 1) are located at ≈211.3 and 208.6 eV, respectively, suggesting that the chemical state of niobium in the NPene@CFC electrode is Nb^{5+} and that no any other chemical states could be found (Figure 3f).[51] At the stage 3 during the negative scan, these two characteristic peaks shifted to a lower energy of 210.1 and 207.4 eV, respectively, owing to the reduction of Nb^{5+} to Nb^{4+}.[52] After the positive scan, all the characteristic peaks of reduction state shifted back to the initial binding energy levels of NPenes in stage 1, demonstrating a reversible redox reaction of Nb^{5+} during the a complete CV scan. Note that no apparent difference has been observed in the XPS peaks of P 2p and O 1s during the charge/discharge process (Figure S19, Supporting Information). This result demonstrates that the energy storage mechanism only involves the reduction and oxidation of Nb^{5+} centers in NPene, and the Nb^{5+} centers contribute to the Faradic pseudocapacitance located near the surface of the NPene at a distance $l \ll \sqrt{2Dt}$, where D is the diffusion coefficient for H^+, and t is time (Figure 3g).[51] Thus the electrochemical reaction could be described as following equation

$$2\left[Nb^{5+}\right]OPO_4 \cdot H_3PO_4 \cdot H_2O + 2xH^+ + 2xe^-$$
$$\rightarrow 2[H_xNb^{(5-x)}]OPO_4 \cdot H_3PO_4 \cdot H_2O \, (x \approx 1)$$

An quasi-solid-state asymmetric supercapacitor (ASC) with NPenes@CFC as the positive electrode, activated carbon (AC)@CFC as the negative electrode,[53] and poly(vinyl alcohol) (PVA)–HCl gel as electrolyte was assembled subsequently, further widening the working potential window of the device up to 2.0 V (**Figure 4**a; Figure S20, Supporting Information). The well-remained CV curves when the scan rate raised to 30 mV s^{-1} demonstrate the excellent performance of the rate capacity of the device (Figure 4b). The specific capacitances of this ASC are calculated based on the GCD results (Figure 4c) to be 219.9, 217.0, 211.4, 194.65, 172.7, 156.9 F g^{-1} at current density of 0.5, 1, 2, 5, 8, 10 A g^{-1}, respectively, with still 71.4% capacitance retention ratio when the current density is 20 times increased compared to the initial value. Calculation for the current density and specific capacitance of the ASC was based on the total mass load of the active materials of both the two electrodes, which was measured by electronic balance for 5 times to reduce the possible accidental errors. The mass load of the active materials for positive electrode and negative electrode in each measurement was 2.4, 2.3, 2.4, 2.5, 2.3 mg and 9.3, 9.6, 9.4, 9.4, 9.5 mg, respectively. Especially, under a high 5 A g^{-1} charge/discharge current density, there is still a capacitance retention
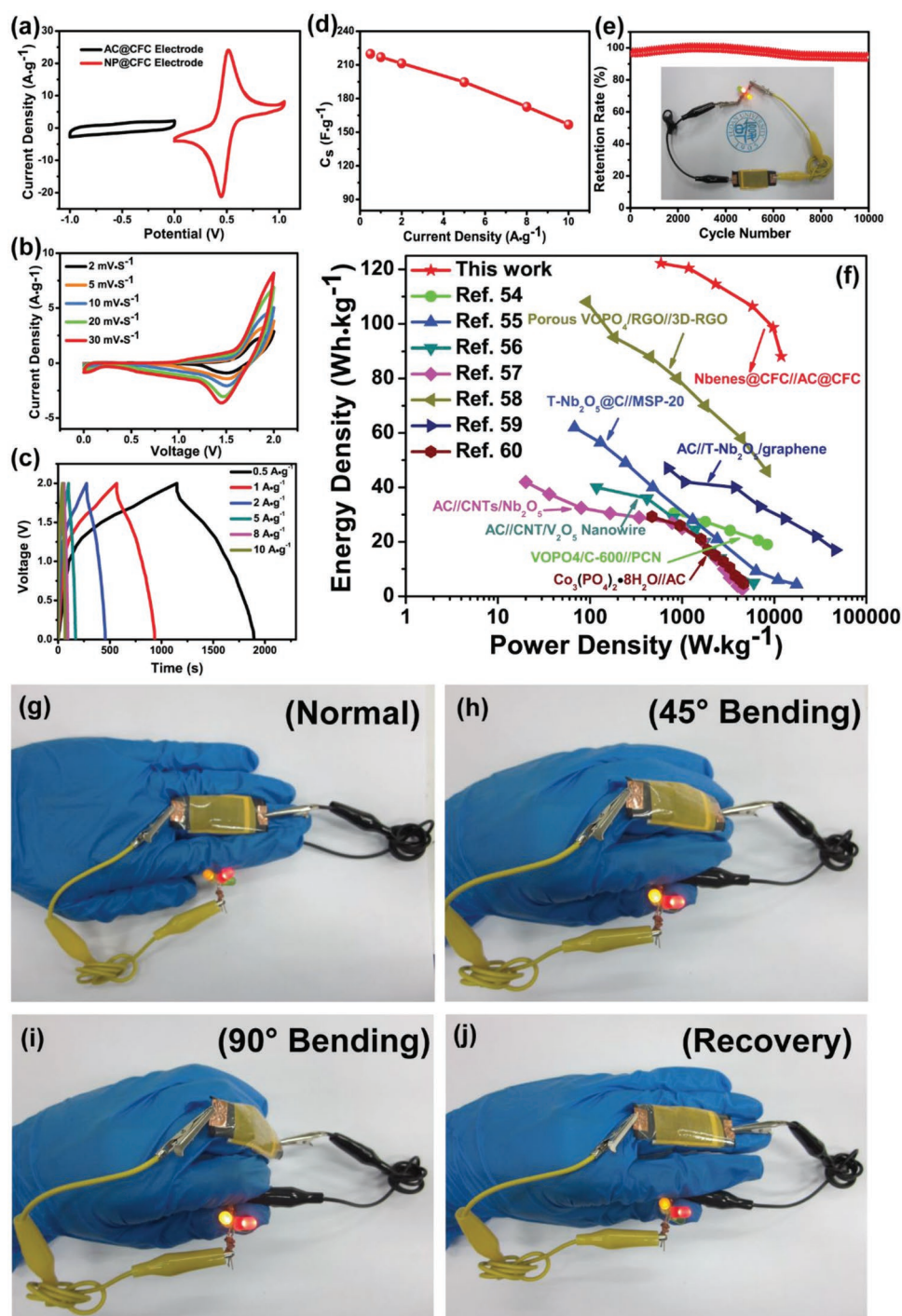
Figure 4. Device performance based on the as-grown NPene@CFC electrode. a) CV curves of the NPenes @CFC and AC@CFC at a scan rate of 10 mV s^{-1}, respectively. b) CV and c) galvanostatic charge–discharge curves of the as-assembled asymmetric NPenes @CFC//PVA–HCl gel//AC@CFC supercapacitor. d) As-calculated C_s of the device at different current densities. e) Cycling performances during 10 000 cycles at a current density of 5 A g^{-1} (insert: image of an LED indictor powered by a piece of fully charged device). f) Performance comparison of other supercapacitors based on various materials. g–j) Photograph of the LED group lighted steadily by the wearable device with a consecutive bending imposed to the flexible device from 0° to 90°.

of 94.2% after 10 000 charge–discharge cycles (Figure 4e). The corresponding SEM image of the electrode after 10 000 cycles (shown in Figure S21, Supporting Information) identify that the 2D nanosheet-like morphology of the nanoarrays was

mostly maintained after the 10 000 cycle test. In addition, the nanosheets after 10 000 cycle shows slightly rough surface with the presence of some small-sized fragments. The device exhibits an energy density of 122.2 W h kg^{-1} at power density

of 589.7 W kg^{-1}, and retains 88.1 W h kg^{-1} at 11 913.9 W kg^{-1}, which surpass most of the solid-state supercapacitors based on other phosphate compounds and similar chemical compounds[54–60] (Figure 4f). We then evaluated the flexibility and wearability of the as-fabricated ASC. A series of light-emitting diodes (LEDs) can operate when a piece of fully charged ASC is attached onto the glove and linked the device with the LEDs indicator. This flexible quasi-solid-state device enables to work as stable power source under either flat or consecutive bent condition (0°–90° and recovered, Figure 4g–j), revealing its excellent flexibility and wearability. The excellent flexibility of the assemble all-solid supercapacitors was further evaluated by the repeated bending tests as shown in Figure S22 in the Supporting Information.[61]

Finally, we confirm that an individual carbon fiber yarn (CFY) ASC based on these NPenes can also be fabricated by the similar strategy (Figure S23, Supporting Information). The NPenes can be in situ grown on an individual 6.5 µm thick carbon fiber yarn, and a CFY device was assembled based on two parallel yarn electrodes were coated with a PVA–HCl gel electrolyte without binder or separator. Also, the typical CV curve with a wide potential window of 2.0 V of the as-fabricated CFYs-based ASC at 2.0 mV s^{-1} was obtained (Figure S23d, Supporting Information), suggesting a possible route for the design and fabrication of the knittable energy storage device based on our ultrathin NPenes.

The high energy storage performance of our NPenes would be attributed to the following aspects: 1) Cation-intercalated energy storage: In general, for most pseudocapacitive materials, the redox reactions are just limited to the surface or near-surface of the electrodes. However, our NPene sheets can greatly utilizes the bulk of electrode material in charge storage through fast intercalation of cations (H$^+$ or Li$^+$), resulting in a high specific capacitance and energy density.[20,21] 2) The enhanced ionicity of Nb—O bond: as theoretically predicted by the previous work, the enhanced ionicity of Nb—O bond with the existence of [PO$_4$]$^{3-}$ group in the present 2NbOPO$_4$·H$_3$PO$_4$·H$_2$O crystal can efficiently produce a high operating voltage window up to 1.0 V.[16–19] 3) The outstanding structure stability of the layered 2NbOPO$_4$·H$_3$PO$_4$·H$_2$O ensure the long-term charge/discharge cycling stability. 4) The typical 2D morphology of the NPenes with atomic thinness of sub-5 nm. This ultrathin thickness should greatly shorten the ion diffusion paths, which are favorable for fast redox reactions and results in good rate performance.[62] 5) In situ growth and binder free design on CFC substrate results in strong affinity and small charge resistance between the substrate and the active materials. This characteristic facilitates the kinetics at the electrode interfaces, exhibiting superior electron mobility during the electrochemical process.[63]

3. Conclusion

In summary, we developed a mild oxalic acid strategy to synthesize the layered niobium phosphate (2NbOPO$_4$·H$_3$PO$_4$·H$_2$O) with typical cation-intercalation pseudocapacitance and high high-voltage (1.0 V) window for electrochemical energy storage. Taking advantage of this strategy, the nanosheet arrays of acid niobium phosphate can be in situ grown on flexible CFC and CFY substrate as flexible, self-standing electrodes for solid-state supercapacitors. The full NPenes @CFC//PVA–HCl gel//AC@CFC ASC exhibited a broad potential window of 2.0 V, a high energy density of 122.2 W h kg^{-1} at a power density of 589.7 W kg^{-1}, and excellent long cycle stability with a capacitance retention of 94.2% after 10 000 cycles. Our findings here could open up a new avenue and a significant step toward exploring 2D niobium phosphate materials with high potential and cation-intercalation pseudocapacitance for flexible energy storage device. Further study based on the exfoliated NPene colloidal solution for other applications, such electrocatalysis and secondary batteries, should be also interesting.

4. Experimental Section

Materials Synthesis and Exfoliation: The 2NbOPO$_4$·H$_3$PO$_4$·H$_2$O bulk were prepared by an oil bath reflux route. In a typical procedure of synthesis, 3.32 g C$_{10}$H$_5$NbO$_{20}$ (98%, w/w) was dissolved in 110 mL deionized (DI) water until the colorless and transparent solution was obtained. The solution was then transferred into a three-necked flask applied with a reflux condenser. Meanwhile, 5 mL phosphoric acid (85%, w/w) was added into a separating funnel equipped up to the flask. The mixed solution was then heated up to 110 °C under a continuous magnetic stirring for 16 h. The phosphoric acid was also added into the heated solution slowly while the heating temperature reaching up to 85 °C. The resulting white product was collected by filtration, washing with DI water and acetone for 5 times, respectively, and eventually dried under vacuum at 60 °C for 8 h. A facile liquid exfoliation process for the 2NbOPO$_4$·H$_3$PO$_4$·H$_2$O bulk can be realized as following operation: after dissolving 10 mg as-prepared bulk in 10 mL DI water and followed by 30 min moderate ultrasonic treatment, a transparent colloidal solution containing monodispersed NPene nanosheets was obtained. The similar exfoliation approach can also be achieved in ethanol solvent.

Materials Characterization: The crystal structure characteristics were studied using a Bruker D8-A25 diffractometer using Cu Kα radiation (λ = 1.5406 Å). For phase identification and structure determination, the synthesized sample was loaded into 0.7 mm quartz capillaries and synchrotron XRPD data were collected using a Mython-II detector at Powder diffraction beamline, Australian Synchrotron. Two separate collections were undertaken at two wavelengths: 0.6884 or 0.5986 Å, determined using NIST SRM 660b LaB$_6$. The high temperature stability was studied using a hot air blower heating up to 900 °C at a ramp rate of 10 °C min^{-1}. In-operando XRPD measurements with cycling of the modified 2032 coin cell in transmission mode was performed using a Neware battery tester system (China). Cells were cycled under a constant current mode with a rate of 0.5 A g^{-1}. Data were collected contiguously with an exposure time of 180 s. TEM, SAED, EDS line scanning and mapping were performed using Philips CM 200 FEG field emission microscope and JEM-2100F Field Emission Electron Microscope, respectively. Zeta-potential test (Zetasizer Nano ZS90) was used to characterize the surface charge state of the nanosheets dispersed in solvents. UV–vis absorption spectroscopy (Hitachi U-3900H Spectrophotometer) was employed to analyze the optical adsorption properties from 200 to 800 nm of the wavelength. The elemental composition and chemical state of the sample were measured using a PHI 5000C EACA system XPS, with a C 1s peak at 284.6 eV as the standard signal. TGA measurements were carried out using a SDT Q600 instrument in a temperature range of room temperature to 1000 °C at a heating rate of 10 °C min^{-1} under air flow.

In Situ Growth of NPenes on CFC: A piece of CFC (10 mm × 35 mm × 0.1 mm, Cetech Co., Ltd.) was pretreated by a mixture of DI water, ethanol and acetone with a mixing ratio of 1:1:1 (v/v) in a moderate ultrasonic environment for 15 min. The CFC was then transferred into a beaker filled with mixed acid of isometric H_2SO_4 (98%, w/w) and HNO_3 (65%, w/w). After a 30 min immerse treatment, the CFC was washed with DI water and ethanol, dried in the oven for 10 min. Before a complete synthesis experiment, the clean and activated CFC was then immersed partially into the aforementioned reaction solution in the three-necked flask system with the help a piece of thread. The reaction system was then carried forward with the same synthesis method. The CFC covered with NPenes nanosheets was finally washed with DI water and ethanol, and then dried in oven at 60 °C for 8 h.

Fabrication of the Quasi-Solid-State Flexible and Wearable ASC: The CFC electrode covered with NPenes nanosheets served as positive electrode of ASC had been fabricated via aforementioned one step in situ growth approach. To fabricate the negative electrode of the device, a piece of CFC with the same size to the positive one was pretreated by the mixture of DI water, ethanol and acetone with a mixing ratio of 1:1:1 (v/v) in a moderate ultrasonic environment for 15 min. The clean CFC was then immersed into the commercial carbonic black ink for 1 min and dried in the oven at 80 °C for 1 h to obtain a layer of active carbon covered on the CFC. PVA gel/HCl electrolyte was obtained by dissolving 3 g of PVA in 30 mL DI water with the assistance of 80 °C heating in a three-necked flask, followed by the addition of 10 mL of hydrochloric acid (37%, w/w) in the procedure of cooling down. As for the fabrication of ASC, the above two electrodes were pressed and combined together with PVA gel/HCl (3 M) as the solid electrolyte to obtain a full ASC. The full ASC was encapsulated by Kapton film with two pieces of copper foil connected to the edge of the two electrodes as the conductive connectors, respectively.

Electrochemical Measurement: The electrochemical measurement for the NPenes@CFC positive electrode was carried out in a three-electrodes system in 3 M HCl aqueous electrolyte. As for the specific procedure, the NPenes@CFC served as the working electrode was soaked in the 3 M HCl aqueous electrolyte for 6 h before the electrochemical measurement. When came to the measurement steps, platinum foil and Ag/AgCl electrode were set as the counter electrode and reference electrode, respectively. The electrochemical properties of the NPenes@CFC//PVA-HCl//AC@CFC quasi-solid-state flexible ASC were examined with two electrodes system, while the NPenes@CFC electrode was used as the positive electrode and the AC@CFC was used as the negative electrode as well as the reference electrode. All of the needed electrochemical measurements including the CV, galvanostatic charge–discharge (GCD), and long-term cycling test were conducted on an electrochemical workstation CHI660E. Electrochemical impedance spectroscopy (EIS) was carried out under the factor of the frequency range from 0.01 Hz to 100 kHz, with an applied AC voltage and DC potential of 10 mV and 0.38 V, respectively. The peak current in the CV curves generally obeys a power–law relationship with the sweep rate

$$i = aV^b \tag{1}$$

where i is the corresponding peak current density at different scan rate, V is the corresponding scan rates varied from 2 to 100 mV s^{-1}, a and b are adjustable values due to the kinetics process. Take the logarithm to the above equation and the resulting one is

$$\log i = b \log V \tag{2}$$

The b values (slope of the tangents at different scan rates) can be calculated according to the above equation.

The calculation method for the capacity contribution is based on the following equation

$$I_p = C_1 \nu + C_2 \nu^{\frac{1}{2}} \tag{3}$$

where I_p (A g^{-1}) is the peak current density at different scan rate, ν (mV s^{-1}) is the specific scan rate, C_1 and C_2 are the corresponding constant

factors of the capacity contribution of surface pseudocapacitive effect and battery-type effect, respectively.

With a deformation of the above equation, the specific contribution rate of different internal mechanisms can be solved according to the following equation

$$\frac{I_p}{\nu^{\frac{1}{2}}} = C_1 \nu^{\frac{1}{2}} + C_2 \tag{4}$$

The specific capacitance of the ASC are calculated from the GCD curves as the following equation

$$C_s = \frac{2 i_m \int V \, dt}{V^2 \Big|_{V_i}^{V_f}} \tag{5}$$

where the C_s (F g^{-1}) is the specific capacitance, current density $i_m = I/m$ (A g^{-1}) with I is the current and the m is mass of the active material, $\int V \, dt$ is the integral area of the discharge curve and the V (V) is the potential with initial and final values of V_i and V_f, respectively.

The specific energy density as well as the specific power density of the ASC are calculated according to the following equations, respectively

$$E = \frac{i_m \int V \, dt}{3.6} \tag{6}$$

$$P = \frac{E}{\Delta t} \times 3600 \tag{7}$$

where E (W h kg^{-1}) is the specific energy density of the ASC, P (W kg^{-1}) is the power density of the device, Δt (s) is the discharge time.

Calculation Method: The plane wave pseudopotential method within DFT as implemented in CASTEP code (V 8.0) was used. The exchange-correlation function was approximated by generalized gradient approximation (GGA) of PBE type. The Hubbard model was used to treat strong on-site Coulomb interaction within the GGA + U method. Ultrasoft pseudopotentials were adopted to describe the core–valence interactions and the wave functions of the valence electrons were expanded in plane waves with a kinetic-energy cutoff of 300 eV. To achieve the accurate density of the electronic states, a 4 × 4 × 4 k-point mesh was used.

Supporting Information

Supporting Information is available from the Wiley Online Library or from the author.

Acknowledgements

Conflict of Interest

The authors declare no conflict of interest.

[1] M. C. LeMieux, Z. Bao, *Nat. Nanotechnol.* **2008**, *3*, 585.

[2] B. D. Gates, *Science* **2009**, *323*, 1566.

[3] D. Yu, K. Goh, Y. Chen, *Nat. Nanotechnol.* **2014**, *9*, 555.

[4] W. Liu, M. S. Song, Y. Cui, *Adv. Mater.* **2017**, *29*, 1603436.

[5] Y. Z. Zhang, Y. Wang, W. Huang, *Chem. Soc. Rev.* **2015**, *44*, 5181.

[6] L. B. Dong, C. J. Xu, X. Zhao, *J. Mater. Chem. A* **2016**, *4*, 4659.

[7] Y. Huang, M. Zhong, C. Y. Zhi, *Nat. Commun.* **2015**, *6*, 10310.

[8] D. Kim, G. Shin, J. S. Ha, *ACS Nano* **2013**, *7*, 7975.

[9] Z. Yang, J. Deng, H. S. Peng, *Angew. Chem., Int. Ed.* **2013**, *52*, 13453.

[10] J. Zang, C. Cao, X. Zhao, *Sci. Rep.* **2014**, *4*, 6492.

[11] Y. H. Lee, Y. Kim, J. W. Choi, *ACS Nano* **2015**, *9*, 12214.

[12] Z. F. Liu, S. Fang, R. H. Baughman, *Science* **2015**, *349*, 400.

[13] P. Simon, Y. Gogotsi, *Nat. Mater.* **2008**, *7*, 845.

[14] W. H. Zuo, C. Y. Xie, J. P. Liu, *Adv. Mater.* **2017**, *29*, 1703463.

[15] P. Barpanda, G. Liu, A. Yamada, *Chem. Mater.* **2013**, *25*, 3480.

[16] C. Z. Wu, X. L. Lu, Y. Xie, *Nat. Commun.* **2013**, *4*, 2431.

[17] N. G. Park, K. M. Kim, S. H. Chang, *Electrochem. Commun.* **2001**, *3*, 553.

[18] C. Masquelier, A. K. Padhi, J. B. Goodenough, *J. Solid State Chem.* **1998**, *135*, 228.

[19] K. S. Nanjundaswamy, A. K. Padhi, J. Yamaki, *Solid State Ionics* **1996**, *92*, 1.

[20] V. Augustyn, J. Come, B. Dunn, *Nat. Mater.* **2013**, *12*, 518.

[21] D. C. Chen, J. H. Wang, M. L. Liu, *J. Am. Chem. Soc.* **2017**, *139*, 7071.

[22] C. B. Zhu, P. Kopold, Y. Yu, *Adv. Mater.* **2016**, *28*, 2409.

[23] Y. J. Fang, Q. Liu, Y. R. Xiao, *Chem* **2018**, *4*, 1.

[24] S. Bruque, M. Martinezlara, J. Sanz, *Inorg. Chem.* **1987**, *26*, 847.

[25] H. M. Zhang, Y. Wang, H. J. Zhao, *ACS Nano* **2016**, *10*, 507.

[26] N. Kinomura, N. Kumada, *Inorg. Chem.* **1990**, *26*, 5217.

[27] X. C. Li, Y. Zhang, G. Z. Lu, *Acta. Phys.-Chim. Sin.* **2012**, *28*, 2349.

[28] L. Moreno-Real, E. R. Losilla, M. A. Gabas, *J. Solid State Chem.* **1998**, *137*, 289.

[29] J. Yamanaka, M. Murai, T. Sawada, *J. Am. Chem. Soc.* **2004**, *126*, 5851.

[30] A. P. Balan, S. Radhakrishnan, P. M. Ajayan, *Nat. Nanotechnol.* **2018**, *13*, 602.

[31] K. Zhang, L. L. Zhang, J. S. Wu, *Chem. Mater.* **2010**, *22*, 1392.

[32] G. P. Wang, L. Zhang, J. J. Zhang, *Chem. Soc. Rev.* **2012**, *41*, 797.

[33] Y. M. He, W. J. Chen, E. Q. Xie, *ACS Nano* **2013**, *7*, 174.

[34] W. Chen, R. B. Rakhi, H. N. Alshareef, *Nano Lett.* **2011**, *11*, 5165.

[35] L. B. Dong, C. J. Xu, Q. H. Yang, *Adv. Mater.* **2016**, *28*, 1675.

[36] C. Z. Yuan, L. Yang, X. W. Lou, *Energy Environ. Sci.* **2012**, *5*, 7883.

[37] S. I. Kim, J. S. Lee, J. H. Jang, *ACS Appl. Mater. Interfaces* **2013**, *5*, 1596.

[38] G. Q. Zhang, H. B. Wu, X. W. Lou, *Energy Environ. Sci.* **2012**, *5*, 9453.

[39] H. C. Chen, J. J. Jiang, D. D. Xia, *Nanoscale* **2013**, *5*, 8879.

[40] L. Wang, Z. H. Dong, J. Jin, *Adv. Funct. Mater.* **2013**, *23*, 2758.

[41] H. L. Wang, H. S. Casalongue, Y. Y. Liang, H. J. Dai, *J. Am. Chem. Soc.* **2010**, *132*, 7472.

[42] H. Chen, L. F. Hu, M. Chen, Y. Yan, L. M. Wu, *Adv. Funct. Mater.* **2014**, *24*, 934.

[43] G. Wee, H. Z. Soh, Y. L. Cheah, S. G. Mhaisalkar, M. Srinivasan, *J. Mater. Chem.* **2010**, *20*, 6720.

[44] K. L. Guo, F. F. Yang, S. Z. Cui, W. H. Chen, L. W. Mi, *RSC Adv.* **2016**, *6*, 46523.

[45] T. Chen, S. Z. Li, J. Wen, P. B. Gui, Y. X. Guo, C. Guan, J. P. Liu, G. J. Fang, *Small* **2018**, *14*, 1700979.

[46] Z. L. Guo, L. Yang, W. Wang, L. X. Cao, B. H. Dong, *J. Mater. Chem. A* **2018**, *6*, 14681.

[47] Q. H. Wang, L. F. Jiao, H. T. Yuan, *J. Mater. Chem.* **2012**, *22*, 21387.

[48] L. Wang, J. J. Liu, H. S. Zhu, *RSC Adv.* **2015**, *5*, 8422.

[49] H. Pang, C. Z. Wei, J. S. Zhang, *Sci. Rep.* **2014**, *4*, 3577.

[50] Y. Gogotsi, R. M. Penner, *ACS Nano* **2018**, *12*, 2081.

[51] A. Sasahara, M. Tomitori, *J. Phys. Chem. C* **2013**, *117*, 17680.

[52] S. H. Li, J. W. Chen, P. S. Lee, *NPG Asia Mater.* **2018**, *10*, 406.

[53] P. P. Shi, R. Chen, W. Huang, *Adv. Mater.* **2017**, *29*, 1703455.

[54] N. N. Chen, J. H. Zhou, W. H. Hou, *Nanoscale* **2018**, *10*, 3709.

[55] E. Lim, C. Jo, J. Lee, *ACS Nano* **2015**, *9*, 7497.

[56] Z. Chen, V. Augustyn, Y. F. Lu, *Adv. Mater.* **2011**, *23*, 791.

[57] X. L. Wang, G. Li, Y. F. Lu, *Adv. Energy Mater.* **2011**, *1*, 1089.

[58] K. H. Lee, Y. W. Lee, J. G. Son, *Sci. Rep.* **2015**, *5*, 13696.

[59] L. P. Kong, C. F. Zhang, D. H. Long, *J. Mater. Chem. A* **2014**, *2*, 17962.

[60] H. Shao, N. Padmanathan, K. M. Razeeb, *ACS Appl. Mater. Interfaces* **2016**, *8*, 28592.

[61] L. B. Dong, C. J. Xu, Q. H. Yang, *Adv. Mater.* **2016**, *28*, 9313.

[62] Z. C. Pan, Y. C. Jiang, L. F. Hu, *ACS Nano* **2018**, *12*, 2968.

[63] P. Y. Yang, Z. Y. Wu, L. F. Hu, *Adv. Energy Mater.* **2018**, *8*, 1801392.